




Role of stacking fault energy in confined layer slip in nanolaminated Cu

Weisen Ji¹, Wu-Rong Jian², Yanqing Su³, Shuozhi Xu^{4,*} , and Irene J. Beyerlein^{5,6}

¹Department of Materials Science and Engineering, University of California, Berkeley, CA 94720-1760, USA

²Department of Mechanical Engineering, Stanford University, Stanford, CA 94305, USA

³Department of Mechanical and Aerospace Engineering, Utah State University, Logan, UT 84322-4130, USA

⁴School of Aerospace and Mechanical Engineering, University of Oklahoma, Norman, OK 73019-1052, USA

⁵Department of Mechanical Engineering, University of California, Santa Barbara, CA 93106-5070, USA

⁶Materials Department, University of California, Santa Barbara, CA 93106-5050, USA

Received: 6 April 2023

Accepted: 14 July 2023

Published online:
27 July 2023

© The Author(s), under exclusive licence to Springer Science+Business Media, LLC, part of Springer Nature 2023

ABSTRACT

Metallic nanolaminates exhibit superior strength compared to their coarsely laminated counterparts. For layer thicknesses in the range of a few to tens of nanometers, the strength of these materials is related to the stress required for individual dislocations to thread through the nanometer-thick layers, a motion called confined layer slip (CLS). Here, using atomistic simulations, we model the CLS in nanolaminated Cu with incoherent interfaces, with a focus on the role of stacking fault energies (SFEs), which are varied by up to one order of magnitude while other material parameters are largely kept the same. Our simulations found that (i) the intrinsic SFE affects the structures of both the dislocation core and the interfaces and (ii) the critical stress for CLS scales positively with the energy of the incoherent interface, but negatively with the ratio between the intrinsic SFE and the unstable SFE.

Introduction

Metallic nanolaminates (MNs) have gained much attention due to the wide range of superior properties they exhibit. Compared to traditional metals with the same composition, MNs have outstanding thermal stability [1], strength [2], ductility [3], as well as resistance to shock [4] and radiation [5]. MNs are

stacks of well-oriented nanometer-thick, metallic layers, alternating in crystallography and/or composition [6, 7]. MNs are widely used in coatings, nanoelectronics, sensing, catalysis, gas separation, and energy-related areas [8–10].

MNs have been shown to demonstrate 3–10× higher strengths than their coarser layered or coarse-grained counterparts. For individual layer

Handling Editor: M. Grant Norton.

Address correspondence to E-mail: shuozhixu@ou.edu

<https://doi.org/10.1007/s10853-023-08779-8>

thicknesses h with nanoscale dimensions, the strength of MNs depends on h , tending to increase as h decreases. Instrumental in understanding their superior strength and layer size h effects on strength is understanding how dislocations move in them and the stresses associated with this motion. For MNs, the main dislocation glide mechanism is thought to depend sensitively on h . Early works have mapped the dislocation slip mechanisms to a range of h , with interface crossing prevailing when $h \approx 1\text{--}2$ nm and confined layer slip (CLS) occurring for few nm $< h <$ tens of nm [11–13]. Experimental evidence of both slip transfer and CLS has been reported in a wide variety of MNs [14–17].

The h range in which most MNs lie is the range wherein CLS dominates. In CLS, the dislocation glides within the nanolayer and as it glides, it must interact with the bounding interfaces. From dislocation theory, it is expected that the dislocation experiences less resistance to glide in the interior of the layer and more resistance at the interfaces. Thus, its morphology in motion is pictured as a dislocation line bowing out in the interior of the layer and line deposition in the boundaries, resulting in their deformation. The former effect is proposed to produce a strength scaling following $\ln(h)/h$ [12]. The latter effect is believed to add extra resistance, depending on the properties of the interface [18].

Because of its characteristic length (< 100 nm), the discrete dislocation dynamics (DDD) and atomistic simulations are ideal tools for modeling CLS. Earlier work of Zbib et al. [19–21] utilized DDD to model CLS in bi-metal Cu/Nb systems (with coherent interfaces) and tri-metal Cu/Ni/Nb system (with both coherent and incoherent interfaces). Their simulations highlighted the significance of the interfacial defect configuration, layer thickness, and volume fractions of constituent materials. In recent years, a few atomistic simulations were devoted to CLS in metallic multilayers, such as nanolaminated Cu [22, 23], nanolaminated Nb [23, 24], and Cu/Nb nanolaminate [23]. It was found that the dislocation gliding mode (e.g., smooth vs. jerky) and minimum resolved shear stress for dislocation glide depend strongly on the chemical compositions of the interface (e.g., segregation of Zr at a Cu GB [22]), chemical compositions of the layers (e.g., Cu vs. Nb [23]), the interfacial structure (e.g., thin vs. thick interface [22]), and the layer thickness (e.g., from 5 to 70 nm [24]).

In face-centered cubic (FCC) metals, the stacking fault energy (SFE) is known to influence the dislocation core structure [25], edge dislocation climb [26], screw dislocation cross-slip [27], deformation twins [28], growth twins [29], grain boundary (GB) energy [30] etc. For Cu, a few sets of interatomic potentials [31, 32] have been developed whereas the intrinsic SFE (ISFE) and/or unstable SFE (USFE) were varied by up to one order of magnitude, while all other material properties were kept almost identical. Using these interatomic potentials, it was found that the SFE plays an important role in collision cascades-induced defect formation [33–37], GB migration [38], dislocation nucleation from GBs [32] and bi-metal interfaces [39], dislocation/Frank loop interactions [40], dislocation/void interactions [31, 41–43], self-interstitials/twin boundary interactions [44], and deformation of a nanotwinned structure [45] in Cu.

Given that the SFE influences both dislocation and interface, it would be interesting to explore how SFE affects CLS, a process that involves a dislocation gliding between interfaces. To our best knowledge, the effect of SFE on CLS remains unexplored. Some unanswered questions are: Does SFE affect CLS simply through its influence on dislocation and interface? Is the role of SFE on dislocation more pertinent than that on interface? The insight gained would benefit the design of strong nanolaminates composed of FCC metals. In this work, we use atomistic simulations to investigate the role of ISFE and USFE in the CLS behavior of dislocations in nanolaminated Cu. Without loss of generality, the edge dislocation and $\{112\}$ interfaces are employed here. Further, the layer thickness is fixed to 5.4 nm, a fine length scale at which dislocations are believed to move via CLS. The interatomic potential developed by Borovikov et al. [32] is employed to assess the effects of both ISFE and USFE on dislocation glide behavior and its initial glide resistance, termed critical resolved shear stress (CRSS) in this paper. We find that the SFEs affect the dislocation structure, interface structure, interface energy, stress–strain responses, and slip resistance. The dislocation glide mode is jerky in all cases and unaffected by variations in SFEs. Apart from a few exceptions, the ISFE and USFE have opposing influences on the CRSS. Increasing ISFE largely lowers the CRSS, while increasing USFE raises it. Therefore, CRSS can be expected to decrease as

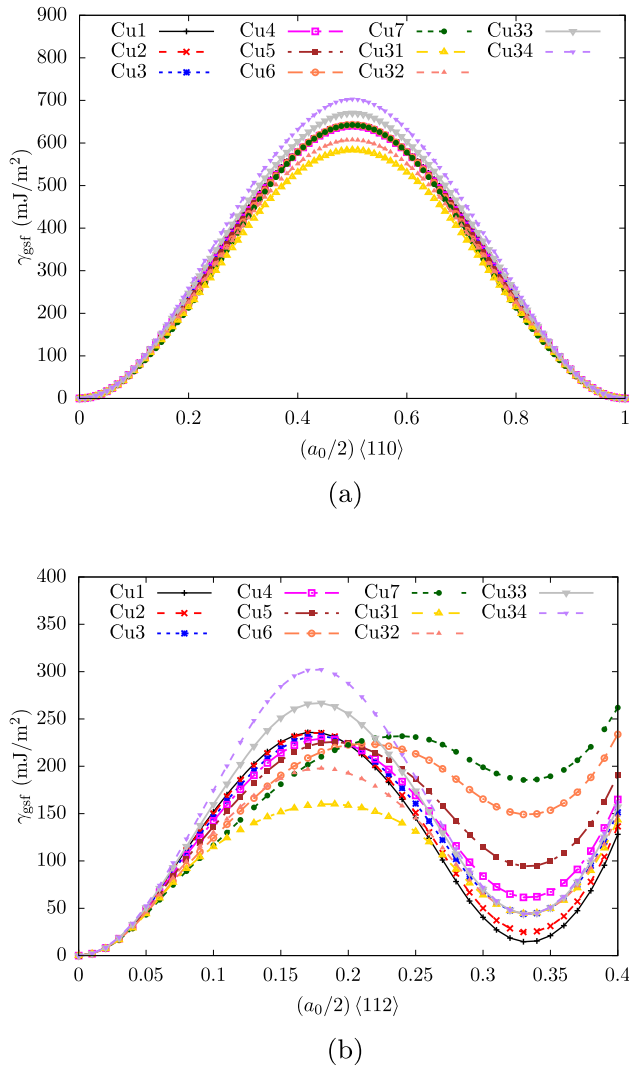


Figure 1 GSFE curves along the **a** $\langle 110 \rangle$ and **b** $\langle 112 \rangle$ in Cu using the eleven EAM potentials [32].

the ISFE/USFE ratio increases. Last, we show that the CRSS increases with the interface energy.

Materials and methods

Interatomic potentials

A set of eleven embedded atom-method (EAM) potentials [32] are employed to help isolate the effects of SFEs on material behavior. The “base” interatomic potential (denoted as Cu3) on which these potentials are built was developed by Mendeleev and King [44] to best represent Cu. Six potentials are produced by first varying the ISFE with a fixed USFE corresponding to Cu (denoted as Cu1, Cu2, and Cu4–Cu7)

[45]. The remaining four potentials correspond to those created by varying the USFE with a fixed ISFE associated with Cu (denoted as Cu31–Cu34) [32]. Other material properties, such as the basic structural parameters, melting temperature, surface energy, point defect formation, and migration energies are nearly identical among the eleven potentials. The lattice parameter, for instance, is either 3.638 Å or 3.639 Å. The values of the three independent elastic constants C_{11} , C_{12} , and C_{44} are 168–180 GPa, 125–131 GPa, and 83–86 GPa, respectively, varying less than 3.5%.

To find the relevant SFEs, the relaxed generalized SFE (GSFE) surfaces are calculated for each of the eleven potentials using procedures described in Ref. [48, 49]. Figure 1 presents the GSFE curves along the $\langle 110 \rangle$ and $\langle 112 \rangle$ directions. Table 1 presents values of ISFE, USFE, and the peak SFE along the $\langle 110 \rangle$ direction γ_{110}^p , calculated for each potential. The ISFE and USFE are the local minimum and local maximum, respectively, on the portion of the $\langle 112 \rangle$ GSFE curve shown in Fig. 1b. As expected, from Cu1 to Cu7, the ISFE steadily increases spanning 170 mJ/m², while the USFE is fixed at around 230 mJ/m². From Cu31 to Cu34, for which the USFE varies while the ISFE is fixed at 44 mJ/m², the USFE increases by 143 mJ/m². Changes in the peak γ_{110}^p among the potentials are small, only increasing slightly with USFE, but nearly unchanged with ISFE. Thus, the key changes within the GSFE surface among these potentials pertain to the ISFE and USFE.

In our earlier CLS study in nanolaminated Cu [23], another interatomic potential by Zhang et al. [46] was used. As a matter of comparison, we note that while it predicts similar ISFE as the base potential Cu3, the lattice parameter is smaller, 3.613 Å, the elastic constants are lower, C_{11} , C_{12} , and C_{44} of 169.9 GPa, 122.6 GPa, and 76.2 GPa, respectively, and the USFE is lower, 161.27 mJ/m² [47]. Thus, we can expect that the dislocation structure, interface energy/structure, and CLS associated with the Zhang potential would be different from those studied here.

Nanolaminate model

Figure 2 shows a schematic of the simulation cell for nanolaminated Cu. The edge lengths of the cell along the x , y , and z directions are 43.7 nm, 10.7 nm, and 25.8 nm, respectively. The cell consists of three layers

Table 1 ISFE, USFE, peak SFE along the (110) direction (γ_{110}^p), interface energy, based on the eleven Borovikov potentials [32] and the Zhang potential [46]

Potential	ISFE	USFE	γ_{110}^p	Interface energy
Cu1	14.63	235.8	643.76	642.88
Cu2	24.89	235.14	640.89	653.76
Cu3	44.1	232.01	640.91	710.37
Cu4	61.54	229.17	640.9	719.32
Cu5	94.41	225.84	643.07	725.51
Cu6	149.16	223.66	643.03	727.27
Cu7	185.55	231.83	642.32	696.79
Cu31	44.43	159.96	583.6	1540.01
Cu32	44.27	197.87	607.3	536.54
Cu33	44.04	266.78	670.26	838.99
Cu34	43.96	302.18	703.16	1494.58
Zhang	43.81 [47]	161.27 [47]	478.32 [47]	467.8 [23]

All energies are in units of mJ/m²

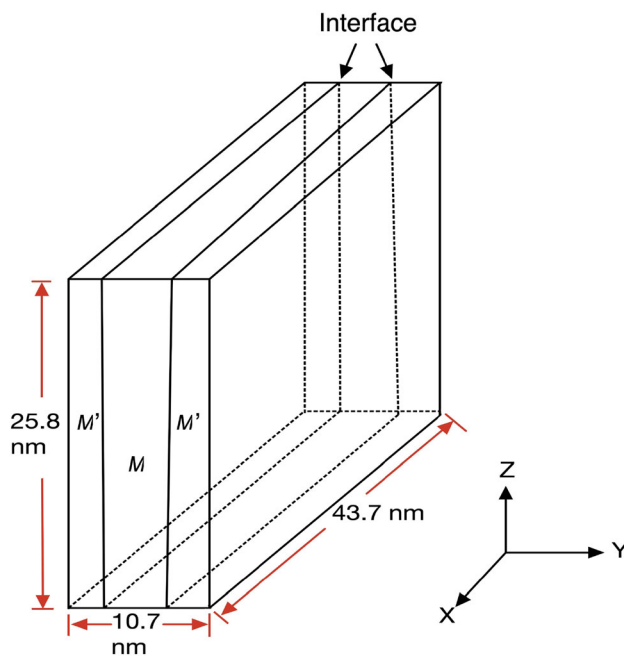


Figure 2 Schematic of the simulation cell for nanolaminated Cu.

along the y direction. The leftmost and rightmost layers have the same crystallographic orientations of $x[1\bar{1}0]$, $y[112]$, and $z[\bar{1}\bar{1}1]$. The central layer, denoted as M , has a crystallographic orientation of $x[1\bar{1}0]$, $y[112]$, and $z[111]$. Periodic boundary conditions are applied in all three directions. As a result, the leftmost and rightmost layers become a single layer (denoted as M') and there are two {112} interfaces in the simulation cell.

Along the y direction, the layers M and M' have the same thickness of 5.4 nm. Prior calculations show that at 1 K, the critical stresses to glide an edge

dislocation between two {112} interfaces spaced by 5 nm, 22–278 MPa [23] are less than that for the same dislocation to transmit across the {112} symmetric incoherent twin boundary (SITB), 100–600 MPa [50]. Therefore, an edge dislocation would glide via CLS in our nanolaminate model.

Stable interface structures

Once the simulation cell is built, a series of operations are conducted to identify the stable interface for each EAM potential. First, layer M is shifted with respect to layer M' along the two in-plane directions, i.e., x and z , to create 100 rigid body translations. In addition, six different cutoff distances (i.e., 0, $0.3a_0$, $0.4a_0$, $0.5a_0$, $0.6a_0$, $0.7a_0$, where a_0 is the lattice parameter) within which one atom is removed from the atom pair within the boundary are considered. As a result, a total of 600 initial structures are built for the nanolaminate. For each structure, energy minimization using the conjugate gradient algorithm is performed [51], before the interface energy is calculated for each energy-minimized boundary using the method in Refs. [23, 24, 52]. The boundary with the lowest interface energy is selected as the stable one.

Dislocation glide simulation

Once the stable interface is determined, an edge dislocation is built into the layer M near the mid- z plane. The dislocation has a slip plane of (111) and a Burgers vector of $[1\bar{1}0]$. Following another energy minimization procedure, a shear strain ϵ_{xz} with a constant rate of 10^7 s^{-1} is applied to drive the edge

dislocation to move along the x direction. The “flexible boundary condition,” as described in Ref. [53], is employed to keep a constant temperature of 1 K and to remove the spurious forces on the dislocation associated with its motion within a small cell. For more details on the simulation set-up, the readers are referred to Ref. [23]. All atomistic simulations in this paper are conducted using LAMMPS [54]. Atomic configurations are visualized using OVITO [55], while defects (e.g., dislocations and interfaces) are identified using the adaptive common neighbor analysis [56].

Results and discussion

Interface structure and energy

All stable interface structures modeled by the eleven EAM potentials are presented in Fig. 3. Ten of the interfaces are SITBs, wherein the structure consists of a repeating unit spanning three $\{111\}$ planes, as depicted in the Cu3 panel. On plane 2, a misfit dislocation dissociates and the stacking fault extends out of SITB by a few Å into the M layer. The length of the extension decreases with increasing ISFE, but is unaffected by changes in USFE. If the edge dislocation is inserted into plane 1 (or plane 3), the extended stacking fault would experience tension (or compression). Due to these distinctions, the CLS of an edge dislocation in these three glide planes is simulated and examined hereinafter. The interface from the Cu7 potential has no misfit dislocations and is coherent.

As mentioned, it has been proposed that the interface energy affects the resistance to CLS. Before discussing CLS results, the effect of ISFE and USFE on the interface energy is examined. Table 1 provides the interface energies from the eleven potentials. Among the ten SITBs, the interface energies are distinct despite similar interface structures. From Cu1 to Cu7 with fixed USFE, the interface energy generally increases with the ISFE, apart from the decrease in interface energy from Cu6 to Cu7, the latter of which corresponds to a coherent interface. From Cu31 to Cu34 with fixed ISFE, no correlation between the interface energy and the USFE is found. The Cu1 and Cu2 potentials achieve the lowest interface energies while the Cu31 and Cu34 potentials the highest ones, although the interface structures based on the four

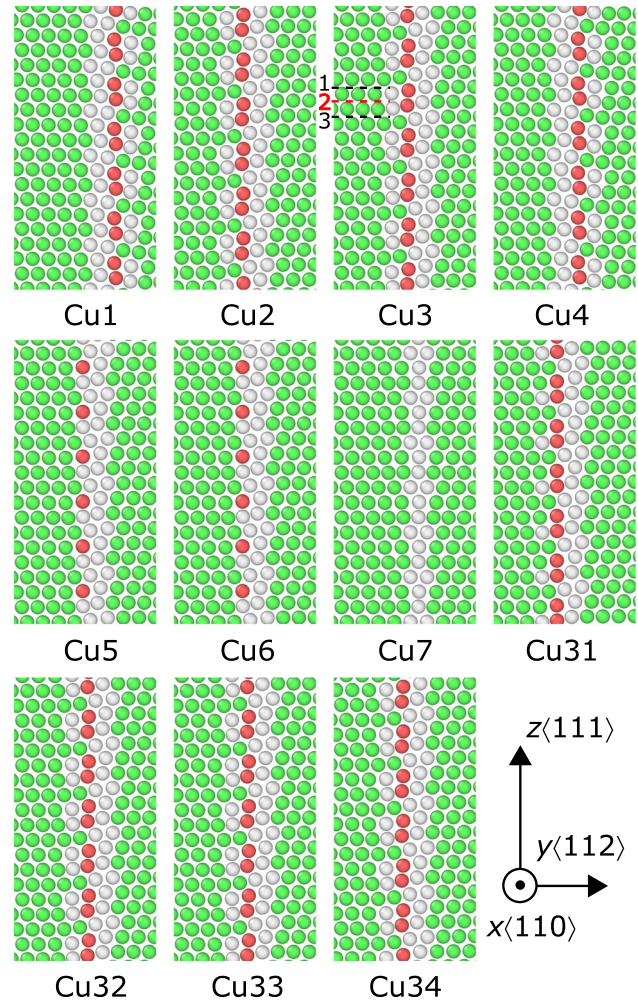


Figure 3 Stable interface structures in Cu using the eleven EAM potentials [32]. Red, green, and white are atoms within local hexagonal close-packed, FCC, and disordered local structures, respectively. Three distinct slip planes within which an edge dislocation can be inserted are shown in the Cu3 panel.

potentials are similar, as shown in Fig. 3. While the Cu7 potential corresponds to a coherent interface, it does not have the lowest interface energy. The ISFE can therefore influence the resistance to CLS by affecting the interface energy.

Stacking fault

Before a driving stress is applied, an edge dislocation is inserted into one of three planes for each potential and then relaxed. In all cases, under no applied stress, the dislocation dissociates and achieves a stacking fault width (SFW) that depends on which of the three planes it lies on and the potential used. These values all deviate from the SFW of the same

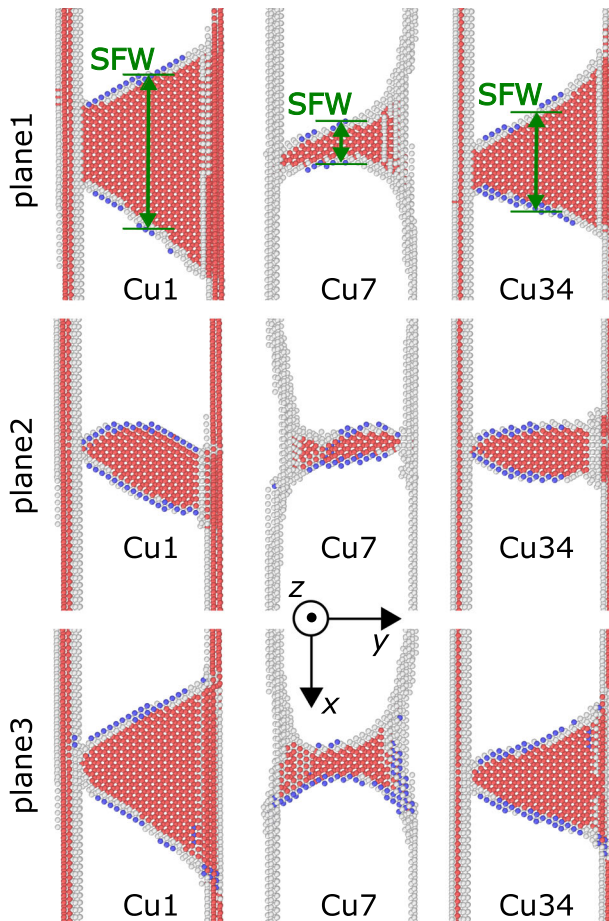


Figure 4 Stable, zero-stress stacking fault structures on different slip planes predicted by the eleven different EAM potentials.

dislocation in a Cu single crystal with the Cu3 potential (3.65 nm). Figure 4 presents selected, zero-stress dislocation structures. The Cu7 potential gives the smallest SFW, which can be expected due to its highest ISFE, and Cu1 the largest SFW, due to its lowest ISFE. The largest SFW is 5.26 nm, which is still smaller than the layer thickness 5.4 nm. Among the three planes, the SFW is the smallest for a dislocation on plane 2, due to direct interaction with the extended misfit dislocation. Also, there is a larger SFW on plane 1 than on plane 3. As further confirmation, the SFW is nearly uniform between the two coherent boundaries (i.e., with no misfits, predicted by the Cu7 potential) among the three planes. Figure 5 shows the variation in the zero-stress SFW with ISFE and USFE. Much like a dislocation in an otherwise perfect single crystal, the SFW decreases with increasing ISFE. When the ISFE is small, the SFW of a dislocation in a single crystal is the largest, and the SFWs among the three planes in the nanolaminate differ greatly. Then,

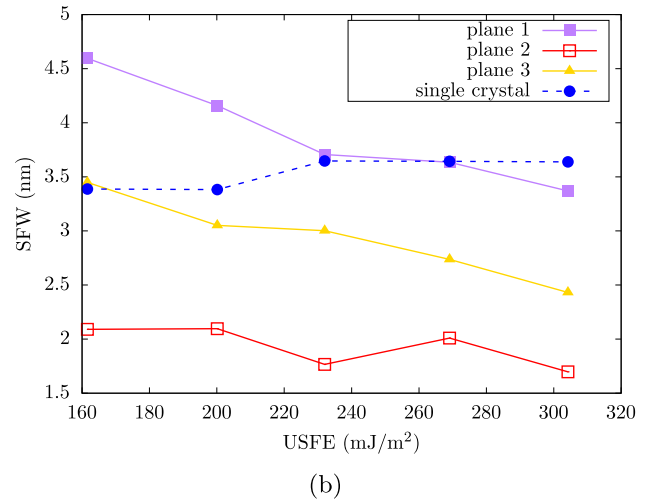
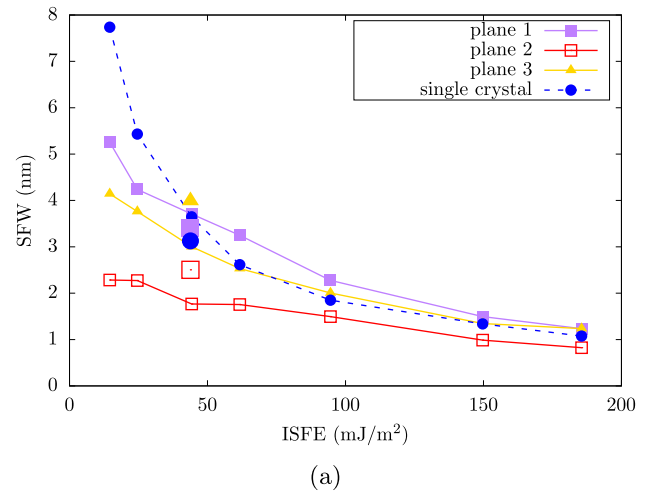


Figure 5 Stress-free SFWs are plotted with respect to **a** ISFE and **b** USFE. In **a**, results using the Zhang potential [46] are denoted by three large symbols.

when the ISFE becomes larger, the differences in SFW among the four cases decrease. This suggests that, for SFW, the interaction between the gliding dislocation and the misfit dislocation becomes less important as the ISFE increases. Compared to the ISFE, the effects of the USFE on the SFW in the nanolaminate are much weaker.

The dislocation structure and interface energy through which it interacts can affect CLS resistance and glide behavior. In the remainder of the analysis, we use “potential + plane” to denote the case with a specific potential (see Table 1) and with the dislocation gliding on a specific slip plane (see the Cu3 panel in Fig. 3). Cu32plane2, for instance, uses the Cu32 potential to model a dislocation gliding on plane 2.

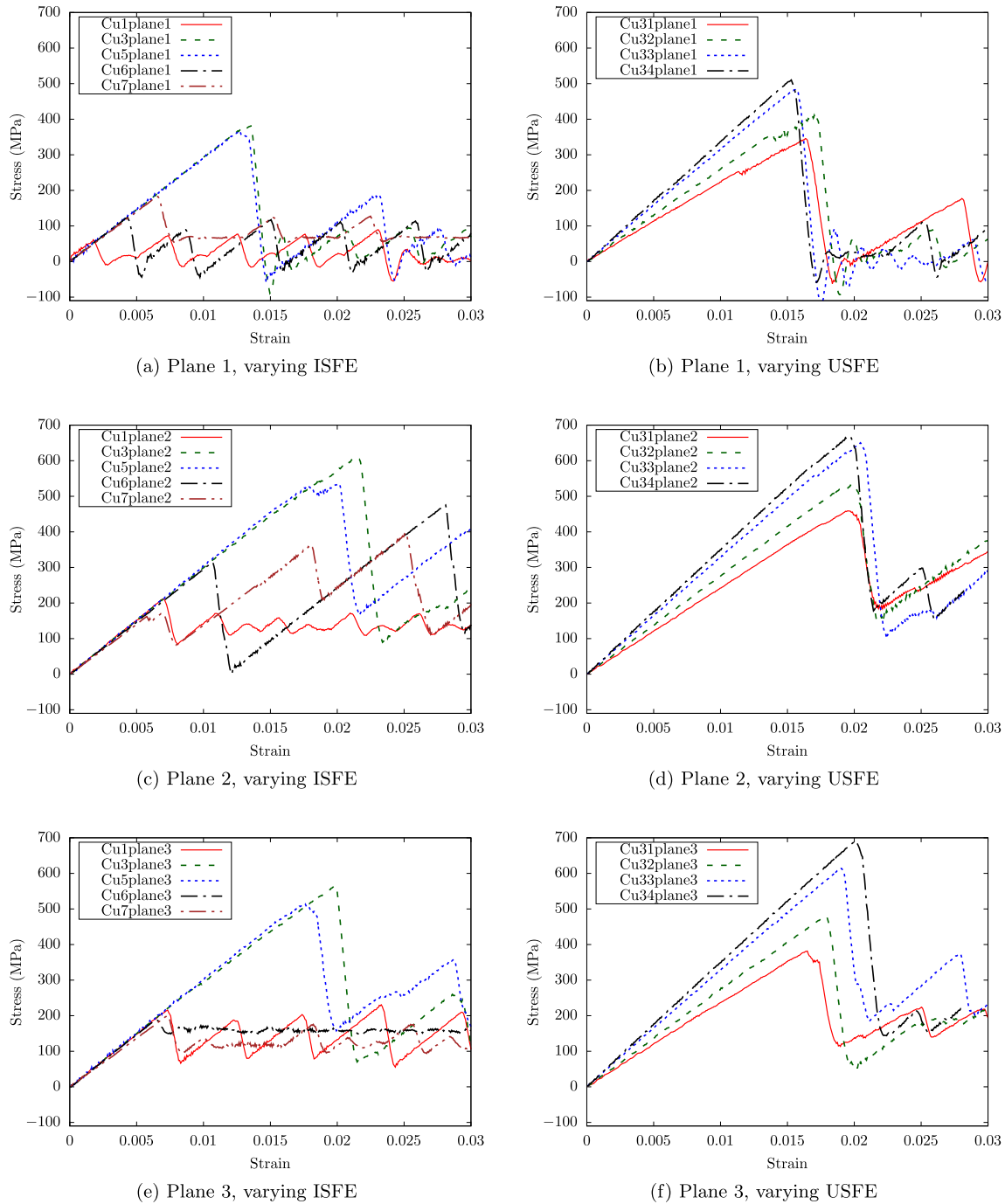


Figure 6 Selected stress–strain curves for the glide of an edge dislocation on three slip planes in nanolaminated Cu. Different interatomic potentials (see Table 1) and slip planes (see the Cu3 panel in Fig. 3) are involved.

Stress–strain response

Figure 6 presents the stress–strain curves corresponding to CLS motion in different planes with different potentials. The shape of the stress–strain curves is similar in all cases. The stress rises linearly as the strain is first applied. In this period, the

dislocation does not move. A local peak stress is reached, corresponding to the moment when the dislocation starts to move in the layer. The stress drops suddenly and then, proceeds to oscillate. The amplitude of the subsequent oscillations generally remains lower than the first peak stress reached.

Thus, the peak stress to initiate motion is considered the CRSS for CLS.

Once the dislocation starts moving, with increasing strain, it does not glide continuously but instead moves back and forth, in a jerky manner, which corresponds to the oscillation in stress seen in Fig. 6. In each oscillation cycle, the forward movement is greater than the backward one, and thus, the net result is that the dislocation still advances forward with straining. This jerky mode of CLS was seen in our prior work [23] for the same layer thickness and SITB, but using another Cu potential. Apart from one case, the dislocation glides on its habit plane.

The only exception is the Cu6plane2 case. In that case, under an applied strain, the misfit dislocation from one SITB extends further into plane 3 until it reaches the other SITB. Then, the edge dislocation on plane 2 partially moves downwards to plane 3, resulting in a dislocation with a jog in the middle. With further straining, the jogged dislocation proceeds to glide in a jerky manner. For more detail, Fig. 7 provides snapshots of various stages in the process. We note that this case has the highest ISFE

and finest SFW among all cases where the misfit dislocations exist. A similar phenomenon was also observed in our prior work for the glide on plane 2 [23].

Variables affecting CRSS

For the wide range of ISFE and USFE studied, we show that these SFEs generally do not affect the form of the stress–strain curve and the mode of CLS glide. In each case, CRSS corresponds to the stress needed to initiate dislocation glide and it is sufficient to sustain CLS with further straining. Also, in all cases, CLS is found to be jerky. The value of the stresses, particularly the CRSS, however, is strongly affected by the dislocation structure and interface energy/structure which can vary greatly depending on the GSFE surface alone. In this section, we examine the effects that these variables have on the CRSS for CLS.

First, we find that the misfit dislocation in the SITB significantly affects the CRSS. Figure 8 presents the CRSS for all cases, by plotting the changes in the CRSS with increasing ISFE (and fixed USFE) or with increasing USFE (and fixed ISFE). The resistance to

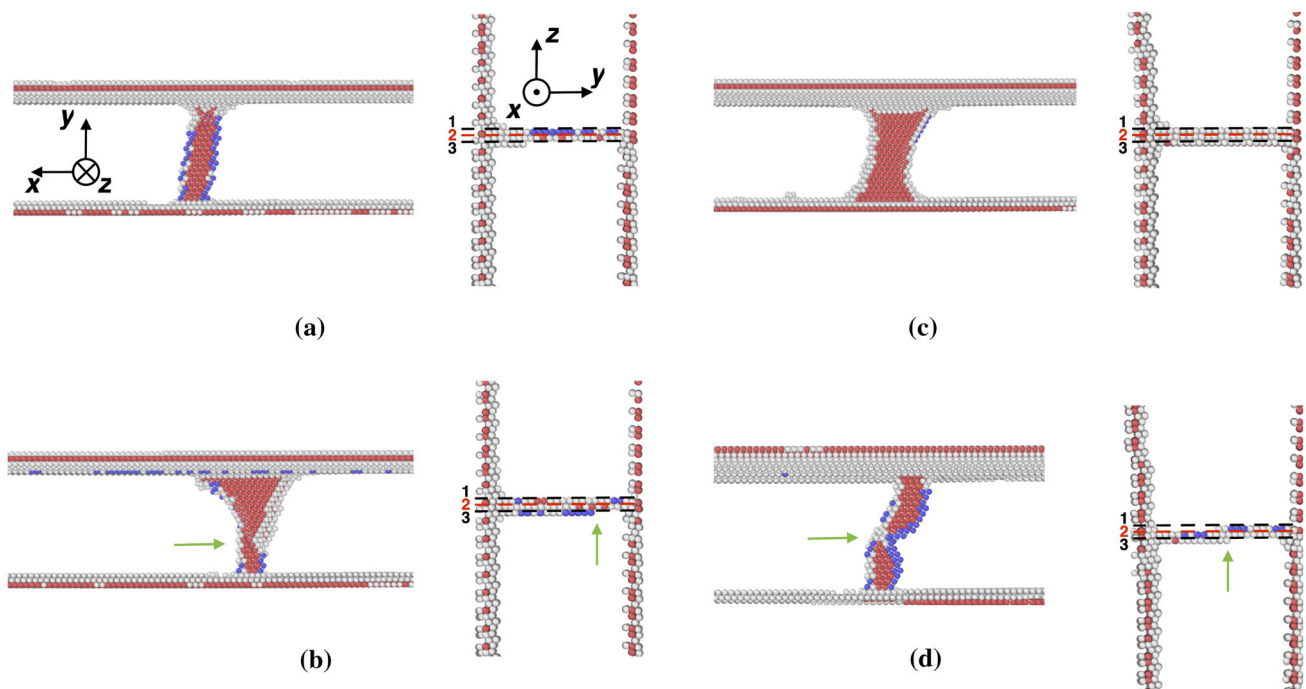


Figure 7 Snapshots of the key processes in the Cu6plane2 case. The dislocation at a strain of **a** 0, **b** 0.0107, **c** 0.01212, and **d** 0.02805. In (a), the edge dislocation is on plane 2. In (b), the dislocation spreads downwards to plane 3. As shown in the right panel, the spreading starts from the left SITB, moves toward the

right, and stops at where the arrow indicates. Between (b) and (c), as the strain increases, the dislocation spreading continues toward the right. In (c), the spreading reaches the right SITB. In (d), as shown in the right panel, the left half of the dislocation is on plane 3 while the right half on plane 2, with the jog denoted by an arrow.

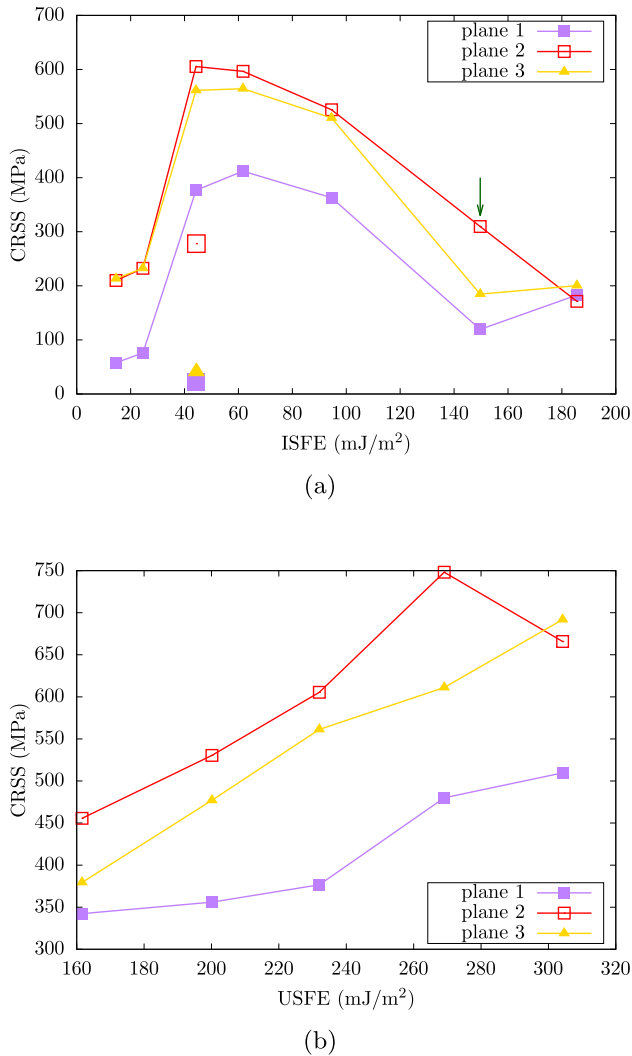


Figure 8 CRSS plotted with respect to **a** ISFE and **b** USFE. The case where the dislocation partially spreads to an adjacent slip plane is marked by an arrow. In (a), results from Ref. [23] using the Zhang potential [46] are denoted by three large symbols.

CLS depends on the glide plane with respect to the misfit dislocation. Plane 2 where the misfit dislocation extends a fault presents the highest resistance to CLS. The gliding dislocation directly intersects the misfits. Although not as direct, moving dislocations on the other two planes still interact with the misfit via elastic interactions. The CRSS to move the edge dislocation in either plane 1 or plane 3 is similar, with plane 3 being slightly more resistant. When the interface is coherent, containing no misfits, the CRSS is similar among the three planes. Therefore, the misfit network gives rise to spatial heterogeneity in CLS, suggesting that the dislocations would prefer to glide in plane 1.

The results in Fig. 8 also imply that the SFEs can affect the CRSS via their effect on the dislocation structure (e.g., the SFW). Previous studies for dislocations in FCC single crystals show that the dislocation slip resistance scales inversely with the SFW [57–59]. For the same potential, the largest SFW is achieved in plane 1. This corresponds to that the CRSS in plane 1 is smaller than that in plane 3.

Figure 8(a) presents the variation in CRSS with ISFE. The CRSS for CLS on all three planes maximizes at the ISFE of 44.1 mJ/m². When ISFE is larger than 44.1 mJ/m², the CRSS drops steadily. There is no expected role of ISFE on the CRSS for CLS and the outcome is likely the result of a combination of factors. As we have shown earlier, ISFE affects the SFW, interface energy, and interface structure. For very low ISFE, the dislocation is wide, which lowers its barrier for glide. As ISFE increases, the misfit dislocation extension reduces in size, which reduces their resistive interaction with the gliding dislocation. The lowest CRSS is achieved for the coherent interface, which has the same CRSS for all three planes. To emphasize the role of interface in CLS, we include in Fig. 8a the CRSS values for the same laminate using the Zhang potential [46], which has the same ISFE as the Cu3 potential, but substantially lower USFE and interface energy (Table 1). The CRSS values are clearly significantly lower, suggesting that USFE and interface energy may underlie any apparent influence of the ISFE.

Results in Fig. 8b indicate that the CRSS scales with the USFE. The USFE varies by up to 143 mJ/m², while the ISFE varies by 0.5% about 44 mJ/m². The positive trend can be expected since the USFE is a local maximum that can be related to the energetic barrier to the Shockley partial motion. While anticipated, it is interesting that the strong influence of the USFE still emerges despite the other coupled effects of the GSFE surface on the gliding dislocation and nanolaminate properties.

Considering all cases together, Fig. 9 shows the variation in CRSS with the ISFE/USFE ratio. Apart from very low ratios, below 0.12, the CRSS decreases with increasing ISFE/USFE. This effect on the CRSS best conveys the main effect of the SFEs found in this work. Smaller USFE will decrease the barrier for Shockley partial glide, while at the same time, larger ISFE reduces the misfit dislocation extensions, both factors that lower the CRSS.

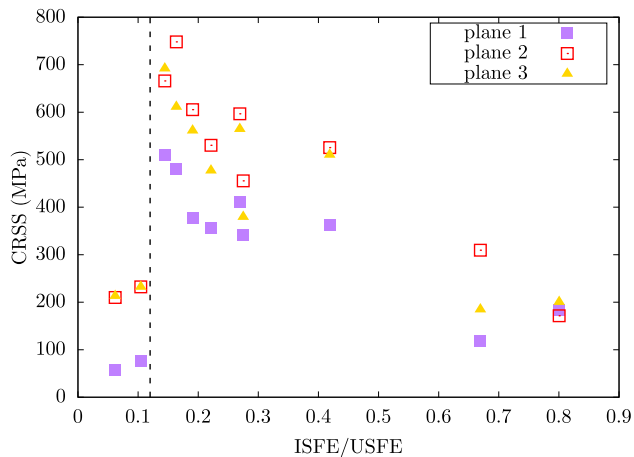


Figure 9 CRSS plotted with respect to the ratio between ISFE and USFE. The dashed vertical line is at $\text{ISFE}/\text{USFE} = 0.12$.

As we have alluded to earlier, the interaction of the dislocation with the interface and the energy of the interface can affect the critical stress for CLS. The glide of dislocation via CLS deforms the boundaries, and it has been proposed that lower energy interfaces pose less resistance to CLS [18]. In agreement, Fig. 10 shows that the resistance to CLS generally reduces as the interface energy reduces. The spread in the CRSS for the same interface is due to the resisting effect of the misfits in the interface. This is an important result of this work. A similar conclusion was reported in a study of incoherent and coherent interfaces in Mg/Nb nanolaminates [60]. Further, these results could explain why general bi-phase metals, which have higher interface energies, are generally stronger than nanotwinned materials [61].

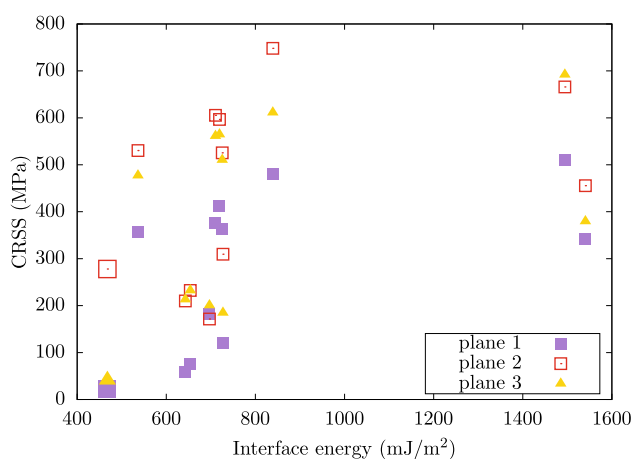


Figure 10 CRSS plotted with respect to the interface energy. Results from Ref. [23] using the Zhang potential [46] are denoted by three large symbols near the left bottom corner.

Conclusions

In this paper, we conduct atomistic simulations to study the effect of SFEs on CLS of an edge dislocation in nanolaminated Cu. The boundaries are $\{112\}$ interface and spaced 5.4 nm apart. We utilize eleven interatomic potentials developed by Borovikov et al. [32], where either the ISFE or the USFE is varied by up to one order of magnitude. The interface intersects with a repeating pattern of three glide planes, distinct in their location with respect to the misfit dislocation. The main findings of this study are as follows:

- The SFWD of the dislocation between two interfaces decreases with an increasing ISFE. In the meantime, the SFWD does not vary much with the USFE.
- The interface energy generally increases with the ISFE but is not correlated with the USFE.
- In all cases, the dislocation glide mode is jerky and unaffected by variations in fault energies.
- With a fixed USFE, there exists an optimal ISFE corresponding to the maximum CRSS for CLS. With a fixed ISFE, the CRSS increases with an increasing USFE. When the ISFE-to-USFE ratio is larger than 0.12, the CRSS decreases with an increasing ratio.
- A larger interface energy can lead to greater CRSS.

The current work made use of a model system and studied the motion of a single dislocation. This would model the case of no pre-strain, where the initial dislocation is sufficiently small that the dislocations can be considered isolated. Prestraining near or beyond the yield point would likely pre-populate the layers with dislocations. Dislocation–dislocation interactions would become important through their individual CLS [24]. We also show that CLS occurs in jerky motion, with frequent stop/starts. Although temperature effects were not studied here, we can anticipate that CLS is a thermally activated mechanism. The additional thermal energy with increases in temperature would facilitate dislocation motion. It has also been suggested that as temperature increases, the transfer of dislocation across the interface becomes easier and thus the layer thickness range over which CLS becomes important reduces [16].

Last, the size effects of layer thickness on CLS were not studied. In our recent work in nanolaminated Nb [24], the increase in CLS resistance is related to

reduced layer thickness, as expected from line tension arguments [62, 63]. For the same reasons, we expect that the critical stress for CLS decreases with increasing layer thickness. However, in Nb, the glide mechanism transitioned as the layer reduced, a result that may be particular to the compact core and interface structure of the body-centered cubic nanolaminate and not transferable to an FCC one.

Acknowledgements

W. J. would like to acknowledge funding in part from the Office of Naval Research under Grant No. N000141712810. S. X. and I. J. B. gratefully acknowledge support by the Department of Energy grant DE-SC0020133 Office of Science, Basic Energy Sciences. Use was made of computational facilities purchased with funds from the National Science Foundation (CNS-1725797) and administered by the Center for Scientific Computing (CSC). The CSC is supported by the California NanoSystems Institute and the Materials Research Science and Engineering Center (MRSEC; NSF DMR 2308708) at UC Santa Barbara.

Author contributions

WJ was contributed to formal analysis, investigation, data curation, visualization, writing—original draft. W-RJ was contributed to conceptualization, methodology, software, validation, writing—review and editing, project administration. YS was contributed to methodology, writing—review and editing. SX was contributed to conceptualization, methodology, validation, writing—original draft, writing—review and editing, visualization, supervision. IJB was contributed to Writing—review and editing, supervision, funding acquisition.

Data availability

The data and code that support the findings of this study are available from Dr. ShuoZhi Xu (email: shuozhixu@ou.edu) upon reasonable request.

Declarations

Conflict of interest The authors declare that they have no known competing financial interests or

personal relationships that could have appeared to influence the work reported in this paper.

References

- [1] Hou J, Li X, Lu K (2021) Formation of nanolaminated structure with enhanced thermal stability in copper. *Nano-materials* 11(9):2252
- [2] Nasim M, Li Y, Wen M, Wen C (2020) A review of high-strength nanolaminates and evaluation of their properties. *J Mater Sci Technol* 50:215–244
- [3] Wang Y, Li J, Hamza AV, Barbee TW (2007) Ductile crystalline-amorphous nanolaminates. *Proc Natl Acad Sci USA* 104(27):11155–11160
- [4] Han WZ, Misra A, Mara NA, Germann TC, Baldwin JK, Shimada T et al (2011) Role of interfaces in shock-induced plasticity in Cu/Nb nanolaminates. *Philos Mag* 91(32):4172–4185
- [5] Beyerlein I, Caro A, Demkowicz M, Mara N, Misra A, Uberuaga B (2013) Radiation damage tolerant nanomaterials. *Mater Today* 16(11):443–449
- [6] Beyerlein IJ, Li Z, Mara NA (2022) Mechanical properties of metal nanolaminates. *Annu Rev Mater Res* 52(1):281–304
- [7] Wang J, Misra A (2011) An overview of interface-dominated deformation mechanisms in metallic multilayers. *Curr Opin Solid State Mater Sci* 15(1):20–28
- [8] Overdeep KR, Livi KJT, Allen DJ, Glumac NG, Weihs TP (2015) Using magnesium to maximize heat generated by reactive Al/Zr nanolaminates. *Combust Flame* 162(7):2855–2864
- [9] Garcia-Pastor FA, Montelongo-Vega JB, Tovar-Padilla MV, Cardona-Castro MA, Alvarez-Quintana J (2020) Robust metallic nanolaminates having phonon-glass thermal conductivity. *Materials* 13(21):4954
- [10] Chavoshi SZ, Xu S (2018) Twinning effects in the single/nanocrystalline cubic silicon carbide subjected to nanoindentation loading. *Materialia* 3:304–325
- [11] Nix WD (1989) Mechanical properties of thin films. *Metall Mater Trans A* 20(11):2217–2245
- [12] Embury JD, Hirth JP (1994) On dislocation storage and the mechanical response of fine scale microstructures. *Acta Metall Mater* 42(6):2051–2056
- [13] Misra A, Verdier M, Kung H, Embury JD, Hirth JP (1999) Deformation mechanism maps for polycrystalline metallic multilayers. *Scr Mater* 41(9):973–979
- [14] Li N, Wang J, Misra A, Huang JY (2012) Direct observations of confined layer slip in Cu/Nb multilayers. *Microsc Microanal* 18(5):1155–1162

- [15] Monclús MA, Zheng SJ, Mayeur JR, Beyerlein IJ, Mara NA, Polcar T et al (2013) Optimum high temperature strength of two-dimensional nanocomposites. *APL Mater* 1(5):052103
- [16] Snel J, Monclús MA, Castillo-Rodríguez M, Mara N, Beyerlein IJ, Llorca J et al (2017) Deformation mechanism map of Cu/Nb nanoscale metallic multilayers as a function of temperature and layer thickness. *JOM* 69(11):2214–2226
- [17] Zheng SJ, Wang J, Carpenter JS, Mook WM, Dickerson PO, Mara NA et al (2014) Plastic instability mechanisms in bimetallic nanolayered composites. *Acta Mater* 79:282–291
- [18] Misra A, Hirth JP, Hoagland RG (2005) Length-scale-dependent deformation mechanisms in incoherent metallic multilayered composites. *Acta Mater* 53(18):4817–4824
- [19] Akasheh F, Zbib HM, Hirth JP, Hoagland RG, Misra A (2007) Dislocation dynamics analysis of dislocation intersections in nanoscale metallic multilayered composites. *J Appl Phys* 101(8):084314
- [20] Akasheh F, Zbib HM, Hirth JP, Hoagland RG, Misra A (2007) Interactions between glide dislocations and parallel interfacial dislocations in nanoscale strained layers. *J Appl Phys* 102(3):034314
- [21] Zbib HM, Overman CT, Akasheh F, Bahr D (2011) Analysis of plastic deformation in nanoscale metallic multilayers with coherent and incoherent interfaces. *Int J Plast* 27(10):1618–1639
- [22] Turlo V, Rupert TJ (2018) Grain boundary complexions and the strength of nanocrystalline metals: dislocation emission and propagation. *Acta Mater* 151:100–111
- [23] Jian WR, Su Y, Xu S, Ji W, Beyerlein IJ (2021) Effect of interface structure on dislocation glide behavior in nanolaminates. *J Mater Res* 36(13):2802–2815. <https://doi.org/10.1557/s43578-021-00261-y>
- [24] Jian WR, Xu S, Su Y, Beyerlein IJ (2022) Role of layer thickness and dislocation distribution in confined layer slip in nanolaminated Nb. *Int J Plast* 152:103239
- [25] Su Y, Xu S, Beyerlein IJ (2019) Ab initio-informed phase-field modeling of dislocation core structures in equal-molar CoNiRu multi-principal element alloys. *Modell Simul Mater Sci Eng* 27(8):084001
- [26] Abu-Odeh A, Cottura M, Asta M (2020) Insights into dislocation climb efficiency in FCC metals from atomistic simulations. *Acta Mater* 193:172–181
- [27] Thornton PR, Mitchell TE, Hirsch PB (1962) The dependence of cross-slip on stacking-fault energy in face-centred cubic metals and alloys. *Philos Mag* 7(80):1349–1369
- [28] Zhang Y, Tao NR, Lu K (2009) Effect of stacking-fault energy on deformation twin thickness in Cu–Al alloys. *Scr Mater* 60(4):211–213
- [29] Velasco L, Hodge AM (2017) Growth twins in high stacking fault energy metals: microstructure, texture and twinning. *Mater Sci Eng A* 687:93–98
- [30] Waters B, Karls DS, Nikiforov I, Elliott RS, Tadmor EB, Runnels B (2023) Automated determination of grain boundary energy and potential-dependence using the OpenKIM framework. *Comput Mater Sci* 220:112057
- [31] Asari K, Hetland OS, Fujita S, Itakura M, Okita T (2013) The effect of stacking fault energy on interactions between an edge dislocation and a spherical void by molecular dynamics simulations. *J Nucl Mater* 442(1):360–364
- [32] Borovikov V, Mendeleev MI, King AH (2016) Effects of stable and unstable stacking fault energy on dislocation nucleation in nano-crystalline metals. *Modell Simul Mater Sci Eng* 24(8):085017
- [33] Yang Y, Okita T, Itakura M, Kawabata T, Suzuki K (2016) Influence of stacking fault energies on the size distribution and character of defect clusters formed by collision cascades in face-centered cubic metals. *Nucl Mater Energy* 9:587–591
- [34] Okita T, Yang Y, Hirabayashi J, Itakura M, Suzuki K (2016) Effects of stacking fault energy on defect formation process in face-centered cubic metals. *Philos Mag* 96(15):1579–1597
- [35] Nakanishi D, Kawabata T, Doihara K, Okita T, Itakura M, Suzuki K (2018) Effects of stacking fault energies on formation of irradiation-induced defects at various temperatures in face-centred cubic metals. *Philos Mag* 98(33):3034–3047
- [36] Hayakawa S, Okita T, Itakura M, Kawabata T, Suzuki K (2019) Atomistic simulations for the effects of stacking fault energy on defect formations by displacement cascades in FCC metals under Poisson's deformation. *J Mater Sci* 54(16):11096–11110. <https://doi.org/10.1007/s10853-019-03688-1>
- [37] Terayama S, Iwase Y, Hayakawa S, Okita T, Itakura M, Suzuki K (2021) Molecular dynamic simulations evaluating the effect of the stacking fault energy on defect formations in face-centered cubic metals subjected to high-energy particle irradiation. *Comput Mater Sci* 195:110479
- [38] McCarthy MJ, Rupert TJ (2020) Shuffling mode competition leads to directionally anisotropic mobility of faceted $\Sigma 11$ boundaries in fcc metals. *Phys Rev Mater* 4(11):113402
- [39] Yao BN, Liu ZR, Legut D, Kong XF, Germann TC, Zhang HJ et al (2021) Cooperative roles of stacking fault energies on dislocation nucleation at bimetal interface through tunable potentials. *Comput Mater Sci* 193:110416
- [40] Hayakawa S, Hayashi Y, Okita T, Itakura M, Suzuki K, Kuriyama Y (2016) Effects of stacking fault energies on the interaction between an edge dislocation and an 8.0-nm-diameter Frank loop of self-interstitial atoms. *Nucl Mater Energy* 9:581–586

- [41] Okita T, Asari K, Fujita S, Itakura M (2014) Effect of the stacking fault energy on interactions between an edge dislocation and a spherical void in FCC metals at various spatial geometries. *Fusion Sci Technol* 66(1):289–294
- [42] Doihara K, Okita T, Itakura M, Aichi M, Suzuki K (2018) Atomic simulations to evaluate effects of stacking fault energy on interactions between edge dislocation and spherical void in face-centred cubic metals. *Philos Mag* 98(22):2061–2076
- [43] Hayakawa S, Doihara K, Okita T, Itakura M, Aichi M, Suzuki K (2019) Screw dislocation-spherical void interactions in fcc metals and their dependence on stacking fault energy. *J Mater Sci* 54(17):11509–11525. <https://doi.org/10.1007/s10853-019-03716-0>
- [44] Mendeleev MI, King AH (2013) The interactions of self-interstitials with twin boundaries. *Philos Mag* 93(10–12):1268–1278
- [45] Borovikov V, Mendeleev MI, King AH, LeSar R (2015) Effect of stacking fault energy on mechanism of plastic deformation in nanotwinned FCC metals. *Model Simul Mater Sci Eng* 23(5):055003
- [46] Zhang L, Martinez E, Caro A, Liu XY, Demkowicz MJ (2013) Liquid-phase thermodynamics and structures in the Cu–Nb binary system. *Model Simul Mater Sci Eng* 21(2):025005
- [47] Xu S, Cheng JY, Li Z, Mara NA, Beyerlein IJ (2022) Phase-field modeling of the interactions between an edge dislocation and an array of obstacles. *Comput Meth Appl Mech Eng* 389:114426
- [48] Xu S, Xiong L, Chen Y, McDowell DL (2017) Comparing EAM potentials to model slip transfer of sequential mixed character dislocations across two symmetric tilt grain boundaries in Ni. *JOM* 69(5):814–821
- [49] Su Y, Xu S, Beyerlein IJ (2019) Density functional theory calculations of generalized stacking fault energy surfaces for eight face-centered cubic transition metals. *J Appl Phys* 126(10):105112
- [50] Ma T, Kim H, Mathew N, Luscher DJ, Cao L, Hunter A (2022) Dislocation transmission across $\Sigma 3\{112\}$ incoherent twin boundary: a combined atomistic and phase-field study. *Acta Mater* 223:117447
- [51] Xu J, Xu S, Beyerlein IJ (2019) Atomistic simulations of dipole tilt wall stability in thin films. *Thin Solid Films* 689:137457
- [52] Xu S, Su Y (2018) Dislocation nucleation from symmetric tilt grain boundaries in body-centered cubic vanadium. *Phys Lett A* 382(17):1185–1189
- [53] Jian WR, Zhang M, Xu S, Beyerlein IJ (2020) Atomistic simulations of dynamics of an edge dislocation and its interaction with a void in copper: a comparative study. *Model Simul Mater Sci Eng* 28(4):045004
- [54] Thompson AP, Aktulga HM, Berger R, Bolintineanu DS, Brown WM, Crozier PS et al (2022) LAMMPS—a flexible simulation tool for particle-based materials modeling at the atomic, meso, and continuum scales. *Comput Phys Commun* 271:108171
- [55] Stukowski A (2009) Visualization and analysis of atomistic simulation data with OVITO—the open visualization tool. *Model Simul Mater Sci Eng* 18(1):015012
- [56] Stukowski A, Bulatov VV, Arsenlis A (2012) Automated identification and indexing of dislocations in crystal interfaces. *Model Simul Mater Sci Eng* 20(8):085007
- [57] Xu S, Mianroodi JR, Hunter A, Svendsen B, Beyerlein IJ (2020) Comparative modeling of the disregistry and Peierls stress for dissociated edge and screw dislocations in Al. *Int J Plast* 129:102689
- [58] Kamimura Y, Edagawa K, Takeuchi S (2013) Experimental evaluation of the Peierls stresses in a variety of crystals and their relation to the crystal structure. *Acta Mater* 61(1):294–309
- [59] Liu G, Cheng X, Wang J, Chen K, Shen Y (2017) Quasi-periodic variation of Peierls stress of dislocations in face-centered-cubic metals. *Int J Plast* 90:156–166
- [60] Wang J, Knezevic M, Jain M, Pathak S, Beyerlein IJ (2021) Role of interface-affected dislocation motion on the strength of Mg/Nb nanolayered composites inferred by dual-mode confined layer slip crystal plasticity. *J Mech Phys Solids* 152:104421
- [61] Subedi S, Beyerlein IJ, LeSar R, Rollett AD (2018) Strength of nanoscale metallic multilayers. *Scr Mater* 145:132–136
- [62] Xu S, Xiong L, Chen Y, McDowell DL (2016) An analysis of key characteristics of the Frank–Read source process in FCC metals. *J Mech Phys Solids* 96:460–476
- [63] Xu S, Su Y, Smith LW, Beyerlein I (2020) Frank–Read source operation in six body-centered cubic refractory metals. *J Mech Phys Solids* 141:104017

Publisher's Note Springer Nature remains neutral with regard to jurisdictional claims in published maps and institutional affiliations.

Springer Nature or its licensor (e.g. a society or other partner) holds exclusive rights to this article under a publishing agreement with the author(s) or other rightsholder(s); author self-archiving of the accepted manuscript version of this article is solely governed by the terms of such publishing agreement and applicable law.